

Fast Inner-Product Algorithms and Architectures for Deep Neural Network Accelerators

Trevor E. Pogue , Nicola Nicolici , *Senior Member, IEEE*

Abstract—We introduce a new algorithm called the Free-pipeline Fast Inner Product (FFIP) and its hardware architecture that improve an under-explored fast inner-product algorithm (FIP) proposed by Winograd in 1968. Unlike the unrelated Winograd minimal filtering algorithms for convolutional layers, FIP is applicable to all machine learning (ML) model layers that can mainly decompose to matrix multiplication, including fully-connected, convolutional, recurrent, and attention/transformer layers. We implement FIP for the first time in an ML accelerator then present our FFIP algorithm and generalized architecture which inherently improve FIP's clock frequency and, as a consequence, throughput for a similar hardware cost. Finally, we contribute ML-specific optimizations for the FIP and FFIP algorithms and architectures. We show that FFIP can be seamlessly incorporated into traditional fixed-point systolic array ML accelerators to achieve the same throughput with half the number of multiply-accumulate (MAC) units, or it can double the maximum systolic array size that can fit onto devices with a fixed hardware budget. Our FFIP implementation for non-sparse ML models with 8 to 16-bit fixed-point inputs achieves higher throughput and compute efficiency than the best-in-class prior solutions on the same type of compute platform.

Index Terms—Algorithms, hardware acceleration, arithmetic complexity

1 INTRODUCTION

RECENT years have seen many works on system-level improvements for machine learning hardware acceleration and hardware-oriented deep neural network (DNN) model optimizations. At a certain point, however, after hardware-oriented DNN model optimizations reach their limit, after the known parallelism and system-level optimizations for executing their compute patterns are exploited, and after technology scaling slows to a halt, there is an accelerator wall which causes limited improvement on the implementation side [1]. A less-explored avenue to continue advancement after this point is to reduce the workload at the algebraic level, by calculating the same machine learning (ML) model algebra, nevertheless using a rearranged compute pattern which produces the same output from fewer or cheaper operations performed in hardware.

This type of arithmetic complexity research has been explored with application to deep learning quite extensively in the case of Winograd's minimal filtering algorithms applied to convolutional neural networks (CNN)s [2] [3]. However, Winograd also introduced an **unrelated and less-explored** algorithm in 1968 on which our work is based that reduces the arithmetic complexity of general matrix multiplication. We refer to this under-explored algorithm from 1968 as the Fast Inner Product (FIP). Compared to the traditional inner product (referred to as baseline), FIP allows matrix multiplication to be performed with approximately half of the multiply-accumulate (MAC) operations traded for low-bitwidth additions. Since MAC units are commonly the area-dominant computational resource in ML accelerators [4] [5] [6], cutting the number of required MAC units in half could nearly double the performance per compute area.

Despite the high impact potential of these benefits, the FIP algorithm [7] has never before been implemented in a machine learning hardware accelerator. The first step in our work is to address this oversight and carry out that investigation. We show that, while the number of required MAC units is nearly halved as expected, there is also a reduction in clock frequency and, as a consequence, throughput.

In order to address this weakness of FIP, we introduce a new inner-product algorithm referred to as the Free-pipeline Fast Inner Product (FFIP) that achieves the same near $2\times$ reduction in required MAC units, however, it inherently improves the clock frequency and, as a consequence, overall throughput for a similar hardware cost compared to FIP. Additionally, as expected from our theoretical analysis, the effective size of the largest systolic array that could be fit in our experimental compute platform was increased from 56×56 processing elements (PE)s when using a baseline systolic array to 80×80 PEs when using (F)FIP systolic arrays, an increase of over $2\times$ in effective number of PEs.

Our work shows that the FFIP architecture is functionally equivalent to traditional systolic array architectures, and that it can be seamlessly incorporated into any ML accelerator system that uses traditional fixed-point systolic arrays for the arithmetic to double the throughput per MAC unit and significantly increase its performance per compute area across all ML models that will execute on the systolic array. This is because any such accelerator could substitute its traditional systolic array PEs for just nearly half the number of proposed FFIP PEs without fundamentally altering the accelerator's functionality or internal interfaces in any way. Furthermore, systolic array accelerators have been proven effective for accelerating a wide range of modern ML models [5] [6] [8] [9] [10]. Our results indicate that FFIP, when overlaid on top of the most efficient systolic array accelerator systems used in practice, can further improve compute efficiency and increase the theoretical performance

- T. E. Pogue and N. Nicolici are with the Department of Electrical and Computer Engineering, McMaster University, Hamilton, ON, L8S 4L8, Canada
Email: poguete@mcmaster.ca; nicolici@mcmaster.ca

limits across a wide range of devices, system implementations, and ML models.

In summary, our key contributions are the following:

- We implement FIP for the first time in a machine learning accelerator and validate our generalized analysis of its ability to increase an accelerator’s theoretical throughput and compute efficiency limits for the data types commonly used in ML acceleration. As part of this undertaking, we also identify a weakness in FIP of a reduction in clock frequency. To address this, we introduce a new inner-product algorithm (FFIP) in Section 3.2 to inherently bypass this trade-off. Additionally, we provide ML-specific optimizations for both the FIP and FFIP algorithms in Section 3.3.
- We propose a generalized PE architecture in Section 4.2 for performing FFIP in hardware which inherently improves the clock frequency and, as a consequence, overall throughput for a similar hardware cost compared to FIP. Additionally, we provide ML-specific hardware optimizations for the systolic array architectures housing FIP or FFIP PEs in Section 4.4. We demonstrate in Section 6 how an example implementation of our abstract FFIP architecture achieves higher throughput and compute efficiency across different ML models than the best-in-class prior solutions implemented on the same type of compute platform. More importantly, the results indicate that when FFIP is overlaid on top of the most efficient systolic array systems used in practice, it can further increase compute efficiency in the general case across a wide range of devices, system implementations, and ML models.

2 RELATED WORK AND BACKGROUND

The architectures evaluated and proposed in this work are systolic arrays, which will also be referred to as matrix multiplication units (MXU)s. Systolic arrays are an effective choice for use in machine learning accelerators as they significantly reduce the required memory traffic and can reach higher clock frequencies than other designs due to the short and regular nature of their interconnects. This type of architecture has been used in state-of-the-art deep learning accelerators such as the Tensor Processing Unit (TPU) [5] [6] [8], among others [9] [10].

2.1 Related Work

The FIP algorithm [7] has been explored by Gustafsson *et al.* for application to finite impulse response (FIR) filtering [11] in a non-systolic-array architecture proposal. Three prior works have also been proposed for systolic array architectures for exploiting FIP [12] [13] [14].

However, none of the prior works on FIP architectures are focused on application to machine learning, which uses a certain range of matrix sizes and data representations, making it deserving of a stand-alone study. For all prior works related to ML acceleration which cite FIP [7], upon closer inspection, it becomes evident that the work either does not evaluate FIP, or the context of the citation is, in fact, referring to Winograd’s more-popular minimal filtering algorithms for convolutional neural networks [2] [3] rather

than Winograd’s inner-product algorithm [7], on which our work is based. Furthermore, the work from Bravo *et al.* [14] reports no clear improvements from their FIP implementation, and all three other prior works on FIP architectures [11] [12] [13] are purely design proposals and do not provide empirical insight into its trade-offs.

The benefits of FIP in hardware rely on the premise that the hardware footprint of adders are cheaper than that of multipliers. Since the arithmetic complexity of fixed-point multipliers scales quadratically with the input bitwidth compared to linearly for adders, this premise has been shown to hold true for fixed-point data types [15] [16] [17]. However, the exact benefits in performance/resources/clock frequency when applying FIP to ML acceleration are still not immediately clear, and finding this out requires a comparison of architecture implementations that use multipliers/accumulators of the specific data sizes/types commonly used in machine learning accelerators.

2.2 Traditional Inner Product (Baseline)

Consider the matrix multiplication $C = AB$ for A of size $M \times K$ and B of size $K \times N$. Using the traditional inner product, C is calculated from MNK multiplications and $MN(K - 1)$ additions, where each element $c_{i,j}$ of C is calculated as follows:

$$c_{i,j} = \sum_{k=1}^K a_{i,k} b_{k,j}. \quad (1)$$

When accelerated on systolic array architectures, the majority of the computational workload in ML models is mapped to matrix multiplication, i.e. Eq. (1), and as can be seen, the operations in this equation are a series of multiply-accumulate operations. For all ML accelerators, unless additional algebraic innovations are used, the throughput is ultimately limited by the maximum number of multiply-accumulate operations from Eq. (1) that can be performed per clock cycle. Therefore, an accelerator’s computational roof is limited by the number of multiplier and adder units it contains.

However, the arithmetic complexity of fixed-point multipliers scales quadratically with the input bitwidth compared to linearly for adders, causing the hardware footprint of fixed-point multipliers to dominate that of adders in the general case [15] [16] [17]. Therefore, multipliers or MAC units are commonly the area-dominant computational resources in ML accelerators [4] [5] [6], and an accelerator’s throughput can be directly limited by how many multipliers its hardware budget can afford. Due to this, surpassing this theoretical performance per multiplier limit has been focused on recently with Winograd’s minimal filtering algorithms applied to convolutional neural networks (CNN)s [2] [3] [4] [18].

In this work, we detail an **under-explored** and extremely competitive alternative to these prior works for surpassing this performance wall and evaluate in-depth how it compares to previous state-of-the-art solutions in Section 6.2.2.

3 FAST INNER-PRODUCT ALGORITHMS

3.1 Fast Inner Product (FIP)

In FIP [7], each element $c_{i,j}$ of C is calculated as follows:

$$c_{i,j} = \sum_{k=1}^{K/2} (a_{i,2k-1} + b_{2k,j}) (a_{i,2k} + b_{2k-1,j}) - \alpha_i - \beta_j, \quad (2)$$

where:

$$\alpha_i = \sum_{j=1}^{K/2} a_{i,2j-1} \cdot a_{i,2j} \quad (3)$$

$$\beta_j = \sum_{i=1}^{K/2} b_{2i-1,j} \cdot b_{2i,j}. \quad (4)$$

Calculating C then requires:

$$\frac{MNK + MK + NK}{2} \quad (5)$$

multiplications for even K and:

$$\frac{3 \cdot MNK + MK + NK}{2} - MN - M - N \quad (6)$$

additions. This means that an accelerator performing this equation instead of Eq. (1) can trade nearly half of its multipliers for low-bitwidth adders while achieving the same throughput. Since the hardware footprint of fixed-point multipliers dominates that of adders [15] [16] [17], FIP can theoretically significantly improve the throughput per compute area roof of an accelerator.

3.2 Free-pipeline Fast Inner Product (FFIP)

This section introduces a new inner-product algorithm referred to as the Free-pipeline Fast Inner Product (FFIP) that, in hardware, achieves the same near $2\times$ reduction in required MAC units as FIP [7] while also addressing a key weakness of FIP by inherently improving the clock frequency and, as a consequence, overall throughput of an accelerator for a similar hardware cost compared to FIP.

In FFIP, each element $c_{i,j}$ of C is calculated as follows:

$$c_{i,j} = \sum_{k=1}^{K/2} g_{i,2k-1}^{(j)} \cdot g_{i,2k}^{(j)} - \alpha_i - \beta_j, \quad (7)$$

where α and β are the same as in Eqs. (3) and (4), and:

$$g_{i,2k-1}^{(j)} = a_{i,2k} + y_{2k-1,j} \quad \text{for } j = 1 \quad (8a)$$

$$g_{i,2k}^{(j)} = a_{i,2k-1} + y_{2k,j} \quad \text{for } j = 1 \quad (8b)$$

$$g_{i,k}^{(j)} = g_{i,k}^{(j-1)} + y_{k,j} \quad \text{for } j > 1 \quad (8c)$$

$$y_{i,j} = \begin{cases} b_{ij} & \text{for } j = 1 \\ b_{ij} - b_{i,j-1} & \text{for } j > 1. \end{cases} \quad (9)$$

The extra subtractions in Eq. (9) require $\Theta(NK)$ operations to calculate, which is negligible since the complexity is dominated by the overall $\Theta(MNK)$ from Eq. (7). Similarly to Eq. (2), Eq. (7) also results in $(MNK + MK + NK)/2$ multiplications for even K and the same number of additions as in Eq. (6) as well.

The resulting terms being multiplied in Eq. (7) are identical to those being multiplied in Eq. (2). The difference between Eqs. (2) and (7) lies in the terms being fed to the addition in Eq. (8c). This allows the addition output $g_{i,k}^{(j)}$ in Eq. (8c) to be passed directly into the adjacent adder for $g_{i,k}^{(j+1)}$, which we later show improves the inner-product's hardware frequency at essentially no cost. Additionally, although each $g_{i,k}^{(j-1)}$ takes $j-1$ iterations to form before being passed to the next $g_{i,k}^{(j)}$, Section 4 shows how these iterations for all g terms in the systolic array are each being performed in parallel in a pipeline every clock cycle. Therefore, after an initial latency that is negligible relative to the entire execution time, every matrix product will thereafter be produced in a pipeline at a consistent throughput.

3.2.1 Proof

For $j = 1$, one can substitute the $g_{i,k}^{(j)}$ and $y_{i,j}$ terms for their values specified in Eqs. (8a), (8b), and (9), and observe the same terms as in Eq. (2). For $j > 1$, Eq. (7) is proven by first showing that Eq. (2) can be rewritten as:

$$\begin{aligned} c_{i,j} &= \sum_{k=1}^{K/2} ([a_{i,2k} + b_{2k-1,j-1}] + [b_{2k-1,j} - b_{2k-1,j-1}]) \\ &\quad ([a_{i,2k-1} + b_{2k,j-1}] + [b_{2k,j} - b_{2k,j-1}]) - \alpha_i - \beta_j \\ &= \sum_{k=1}^{K/2} (h_{i,2k-1}^{(j-1)} + y_{2k-1,j}) (h_{i,2k}^{(j-1)} + y_{2k,j}) - \alpha_i - \beta_j, \end{aligned} \quad (10)$$

where:

$$h_{i,2k-1}^{(j-1)} = a_{i,2k} + b_{2k-1,j-1} \quad (11a)$$

$$h_{i,2k}^{(j-1)} = a_{i,2k-1} + b_{2k,j-1}, \quad (11b)$$

and therefore:

$$h_{i,2k-1}^{(j)} = a_{i,2k} + b_{2k-1,j} \quad (12a)$$

$$h_{i,2k}^{(j)} = a_{i,2k-1} + b_{2k,j}. \quad (12b)$$

Now, $h_{i,2k-1}^{(j)}$ and $h_{i,2k}^{(j)}$ can also be rewritten as:

$$\begin{aligned} h_{i,2k-1}^{(j)} &= (a_{i,2k} + b_{2k-1,j-1}) + (b_{2k-1,j} - b_{2k-1,j-1}) \\ &= h_{i,2k-1}^{(j-1)} + y_{2k-1,j} \end{aligned} \quad (13a)$$

$$\begin{aligned} h_{i,2k}^{(j)} &= (a_{i,2k-1} + b_{2k,j-1}) + (b_{2k,j} - b_{2k,j-1}) \\ &= h_{i,2k}^{(j-1)} + y_{2k,j}. \end{aligned} \quad (13b)$$

Therefore, $h_{i,k}^{(j)} = h_{i,k}^{(j-1)} + y_{k,j}$ and holds the equivalent property as Eq. (8c), showing that $h_{i,k}^{(j)} = g_{i,k}^{(j)}$ and that Eq. (10), which is equivalent to Eq. (2), is equivalent to:

$$\begin{aligned} c_{i,j} &= \sum_{k=1}^{K/2} (g_{i,2k-1}^{(j-1)} + y_{2k-1,j}) (g_{i,2k}^{(j-1)} + y_{2k,j}) - \alpha_i - \beta_j \\ &= \sum_{k=1}^{K/2} g_{i,2k-1}^{(j)} \cdot g_{i,2k}^{(j)} - \alpha_i - \beta_j, \end{aligned} \quad (14)$$

which is equivalent to Eq. (7).

3.3 Machine-Learning-Specific Optimizations

For the application of FIP and FFIP to machine learning, a values represent the layer inputs of a DNN layer, b values represent the layer weights, and c values correspond to the layer's output values. The β term in the FIP and FFIP algorithms is a function of the weights. Hence, it remains constant over each inference and can be pre-computed after training. The β terms can also be incorporated into the biases, allowing the β subtraction in Eq. (2) to be performed during the bias addition stage at no extra cost. Each β_j term is then subtracted from $bias_j$ as follows:

$$bias_j = bias_j - \beta_j, \quad (15)$$

where each j represents a layer output channel. This allows the computation from Eq. (7) to be reduced to:

$$c'_{i,j} = \sum_{k=1}^{K/2} g_{i,2k-1}^{(j)} \cdot g_{i,2k}^{(j)} - \alpha_i, \quad (16)$$

where c' is a layer output before biasing and activation.

Finally, the $y_{i,j}$ values in FFIP from Eq. (9) are also a function of the layer weights, and can also be pre-computed after training.

4 FAST INNER-PRODUCT ARCHITECTURES

4.1 Definitions

- w : The bitwidth that the weight and activations are quantized to.
- d : A bitwidth increase applied to certain locations in the FIP and FFIP PE datapaths, where $d = 1$ if a and b are both signed or both unsigned, and $d = 2$ if either a or b is signed while the other is unsigned.
- X, Y : The width and height of an MXU, respectively, in effective number of MAC units. For a baseline MXU, this refers to the actual width and height in number of MAC units. For FIP and FFIP MXUs, X and Y refer to the MAC width and height required to achieve the same computational power if implemented on a baseline MXU. However, for FIP and FFIP, the number of actual instantiated MAC columns is $X/2$, and the number of actual instantiated MAC rows is $Y + 1$ (where the extra row is for calculating the α terms as explained in Section 4.3).

4.2 Processing Element (PE) Architectures

Fig. 1a shows two traditional PEs which implement the baseline inner-product algorithm as in existing state-of-the-art systolic array ML accelerator architectures [5] [6] [8] [9] [10]. Figs. 1b and 1c show PE architectures for implementing the FIP and FFIP algorithms in an MXU hardware architecture, respectively. The FIP and FFIP PEs shown in Figs. 1b and 1c each individually provide the same effective computational power as the combined computational power of the two baseline PEs shown in Fig. 1a which implement the baseline inner product.

As can be seen, compared to the baseline PEs, the FIP and FFIP PEs therefore provide the same computational

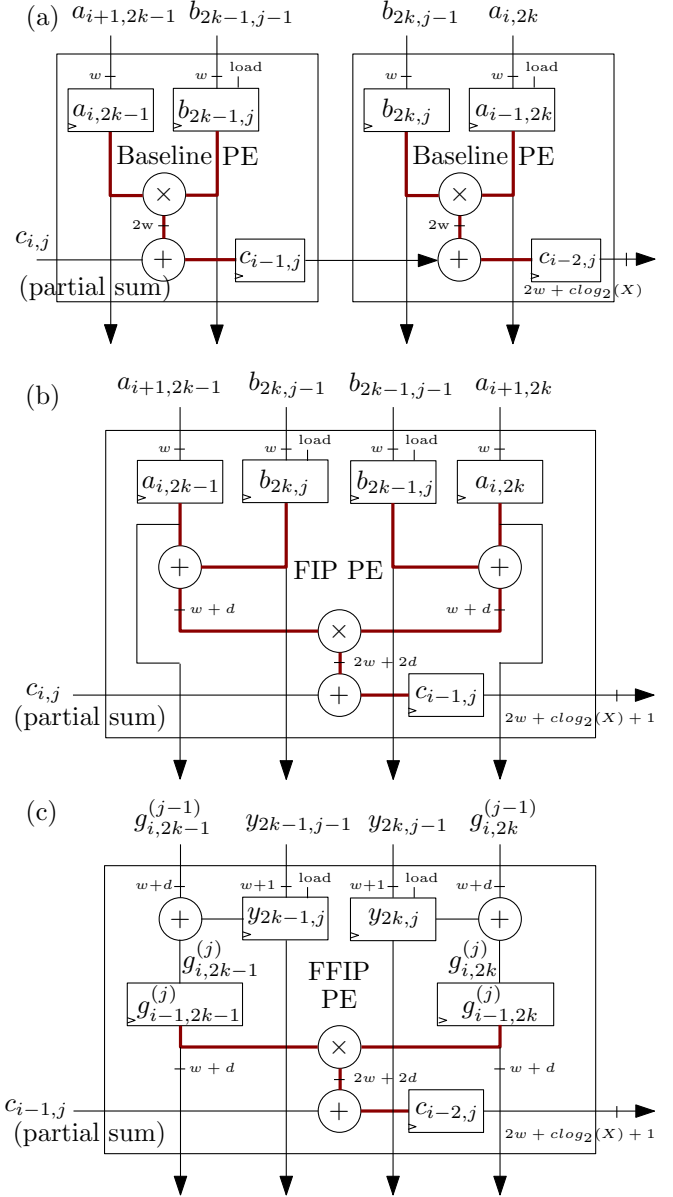


Fig. 1: The PE architectures for implementing the (a) baseline, (b) FIP, and (c) FFIP algorithms in hardware. The FIP and FFIP PEs shown in (b) and (c) each individually provide the same effective computational power as the two baseline PEs shown in (a) combined which implement the baseline inner product as in existing systolic array ML accelerators. Critical paths are highlighted.

power with half the number of multipliers, where the removed multipliers are instead traded for cheap additions on w or $w + d$ bits. Furthermore, half of the accumulations on $2w + clog_2(X)$ bits are also traded for lower-bitwidth additions on w or $w + d$ bits. Finally, one last benefit is that the MXUs using FIP and FFIP PEs have a latency that is $X/2$ fewer clock cycles than a baseline MXU.

The resulting terms being multiplied in Fig. 1c are the same as in Fig. 1b, however, the addition outputs $g_{i,k}^{(j)}$ (the elements $g_{i-1,2k-1}^{(j)}$ and $g_{i-1,2k}^{(j)}$ in Fig. 1c) can now be passed directly into the adder inputs of the next adjacent PE below.

This is beneficial because the addition outputs $g_{i,k}^{(j)}$ stored in registers now serve the dual purpose of:

- 1) Acting as pipelining registers for the addition outputs in Eq. (8), allowing the $g_{i,k}^{(j)}$ terms to be buffered directly before the multiplication, and
- 2) Serving as systolic buffers to store the $g_{i,k}^{(j)}$ input for the adjacent PE below.

In contrast, the FIP algorithm from Eq. (2) requires the inputs (a and b in this case) to be stored in systolic buffers prior to addition before passing them to the adjacent PEs below, but doing so does not serve the dual purpose of also acting as pipelining registers before the multiplication. Therefore, the FFIP algorithm inherently results in a higher maximum frequency for a similar hardware cost.

However, in order to facilitate the usage of the FFIP PEs and gain their benefits, it is mandatory to fundamentally change the systolic array data flow of the original FIP algorithm in a non-obvious way requiring a high-level mathematical understanding of the algebra being performed, and is something that goes beyond the capabilities of today's CAD tools. Our FFIP algorithm defined in Section 3.2 provides these required high-level mathematical changes.

4.2.1 FFIP PE versus FIP PE with Additional Registers

After investigating and implementing the FIP algorithm in hardware, a key downside we found was that the FIP implementation results in a reduction in clock frequency and, as a consequence, throughput in the resulting architecture. As illustrated in Fig. 1b, this reduction in clock frequency comes from the fact that the longest path between registers that the logic in the FIP PE has to traverse through is across two adders and one multiplier rather than just one adder and multiplier. While additional registers could be placed at the FIP PE multiplier inputs to match the critical path of the FFIP PE, this adds a significant cost in registers in the PE array compared to using FFIP. The register requirements for each FIP PE would then increase from Eq. (17) to Eq. (18):

$$4w + (2w + \text{clog}_2(X) + 1) = 6w + \text{clog}_2(X) + 1 \quad (17)$$

$$2(w + d) + (6w + \text{clog}_2(X) + 1) \quad (18a)$$

$$= 8w + 2d + \text{clog}_2(X) + 1, \quad (18b)$$

where Eq. (18) is derived by adding to Eq. (17) the register sizes that would be required to buffer the multiplier inputs. In contrast, the register requirements for each FFIP PE is:

$$2(w + d) + 2(w + 1) + (2w + \text{clog}_2(X) + 1) \quad (19a)$$

$$= 6w + 2d + \text{clog}_2(X) + 3. \quad (19b)$$

Fig. 2 shows that the FFIP register overhead defined in Eq. (19) starts to increase more rapidly for bitwidths below 4, which may make it less desirable to use below that width. However, outside of this range, FFIP register requirements are significantly less than an FIP PE with extra registers added to match the critical path/frequency of an FFIP PE.

Finally, while there will also be other registers to consider in an accelerator outside of the PEs in the datapath and control logic, these register utilizations are highly implementation-specific and will vary depending on the

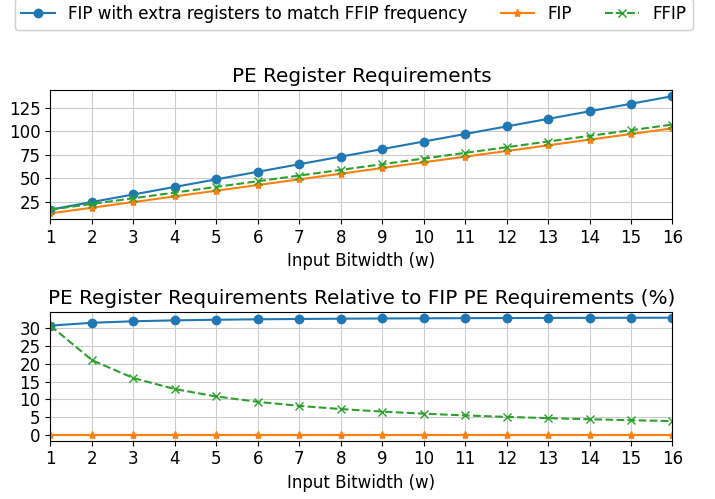


Fig. 2: PE register requirements at different w bitwidths for the FIP PE, FFIP PE, and FIP PE with extra registers before the multiplier to match the frequency of the FFIP PEs. Values are calculated using Eqs. (17) - (19) for $X = 64$ and $d = 1$.

details of the system implementation used to house the systolic array. Furthermore, as the systolic array size increases, the number of PEs increase quadratically and their total register contributions determined by Eqs. (17), (18), or (19) will dominate other registers outside of the systolic array.

4.3 Matrix Multiplication Unit (MXU) Architectures

Fig. 3 shows how the PEs are laid out into an MXU architecture. The suggested MXU input buffers shown are triangular-shaped register arrays containing X shift registers of varying depths, with each shift register SR_k loading one $a_{i,k}$ or $b_{k,j}/y_{k,j}$ value per clock cycle. The depth of each SR_k is $\lceil k/2 \rceil$ for the FIP and FFIP MXUs, and k for the baseline MXU. In order to perform general matrix multiplication (GEMM) on a MXU, the input matrices are divided into tiles fed to the MXU one-by-one. Following each tile multiplication, the partial tile products are accumulated outside of the MXU to generate each final matrix product tile. Prior to each tile multiplication, a b/y tile is loaded into the MXU. It then remains in place as the a/g tile flows through the MXU producing the tile product, during which a new a_i vector is fed into the MXU each clock cycle. Additionally, to hide the latency of loading b/y tiles, we suggest the MXU contains an extra b/y tile buffer which loads the next tile as the current tile is being multiplied.

4.4 Machine-Learning-Specific Optimizations

In quantized ML inference, the weights and activations can each be quantized to signed or unsigned integers by choosing different zero points to quantize the values with [19]. However, for the FIP and FFIP architectures it is beneficial to quantize the weights and activations such that they are *both* represented on either signed or unsigned integers. Otherwise, representing one on signed and the other on unsigned adds a penalty in the hardware footprint of the FIP and FFIP PEs because then, due to the possible range of the result, d must equal 2 instead of 1, and the sum of a and

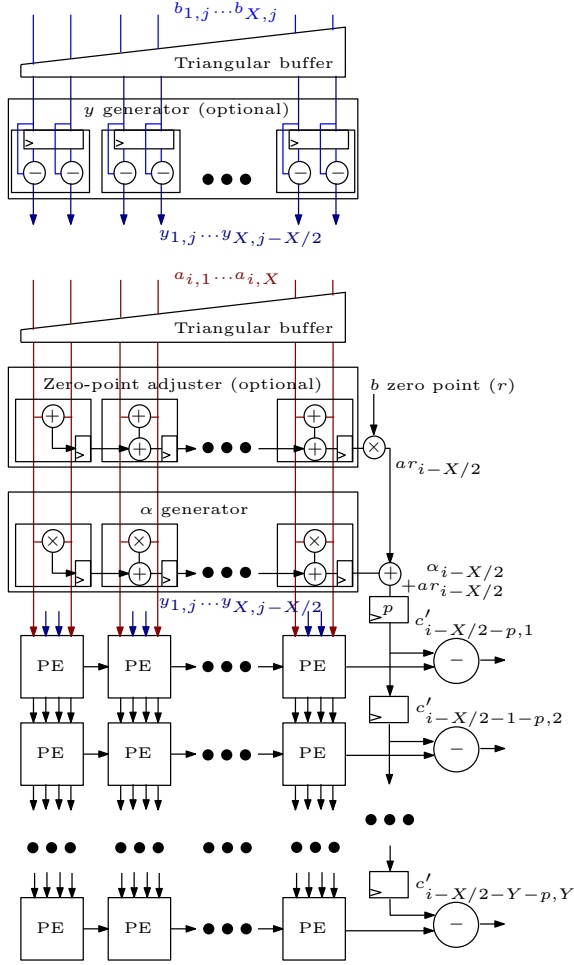


Fig. 3: The FFIP MXU architecture. The FIP MXU is the same except that FIP PEs are used instead and the y generator block is not present, and b inputs are passed in instead of y inputs. The α terms are calculated and subtracted as shown by first passing the a inputs through an additional row of MAC units before they enter the rest of the MXU.

b elements must then be represented on $w + 2$ bits rather than the $w + 1$ bits needed if they were both signed or both unsigned. This would lead to extra register requirements in the FFIP PE and cause multiplication on $w + 2$ -bit inputs rather than $w + 1$ bits for both the FIP and FFIP PEs.

Furthermore, if the employed quantization scheme uses nonzero zero points for the weights, the contributions of the zero points in the GEMM product must then be separately calculated and subtracted from the result to eliminate their contribution (for any architecture, not just FIP and FFIP) [19]. We provide a solution to mitigate this penalty in the FIP and FFIP architectures when layer-wise zero points are used on the weights. We show how to pass some of these extra required computations into the pre-existing α generator logic as shown in Fig. 3. To help illustrate how this works, consider that the weight zero points can be represented by a constant matrix R being added to the weights where each element has a constant value. This results in the MXU performing the following computation:

$$A(B + R) = AB + AR. \quad (20)$$

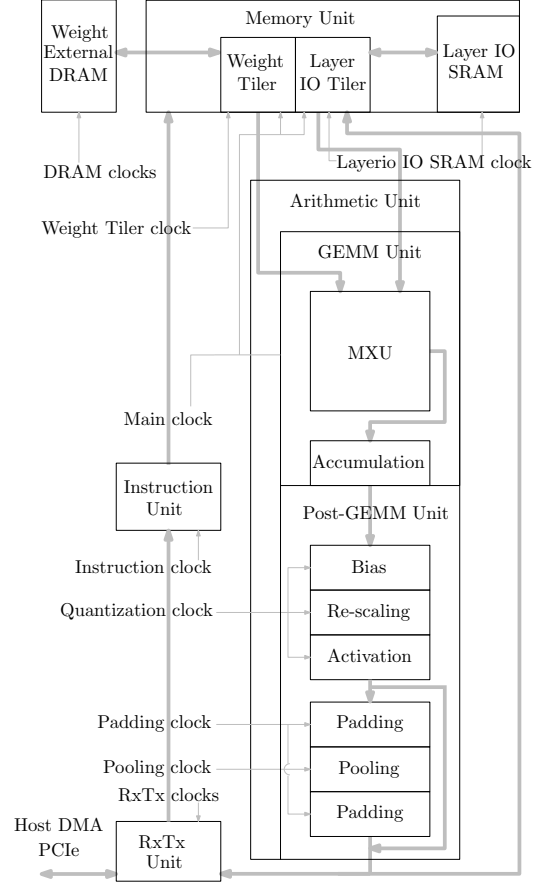


Fig. 4: The example accelerator system design used to host and evaluate the baseline, FIP, and FFIP MXUs when overlaid on top of systems based on the most efficient systolic array accelerators used in practice, e.g., the TPU [5] [6] [8].

Therefore, in order to eliminate the contribution of the constant matrix R in the matrix product, the AR product must be subtracted from the MXU output. In order to do this and combine its subtraction with the existing α generator logic, we provide the *zero-point adjuster* block shown in Fig. 3, which calculates the AR elements using only one multiplier, and show how to efficiently combine its AR output elements with the α elements. This way, both the AR and α values are subtracted from the MXU output vectors at the same time and an additional hardware subtraction vector dedicated to subtracting only the AR elements is not required on the MXU output.

Finally, as discussed in Section 3.3, the β terms do not need to be calculated as they do for α since they can be pre-computed and added to the biases. Furthermore, the y values can either be calculated in real time with the y generator as shown in Fig. 3, or they can be pre-computed at the cost of storing them in 1 extra bit in memory.

5 SYSTEM ARCHITECTURE

The key contributions of this work are the proposed FFIP algorithm and architectures and their application to ML acceleration, which improve the under-explored FIP [7] that has never before been applied to ML acceleration. However, in order to ensure that there are no unseen side-effects, it

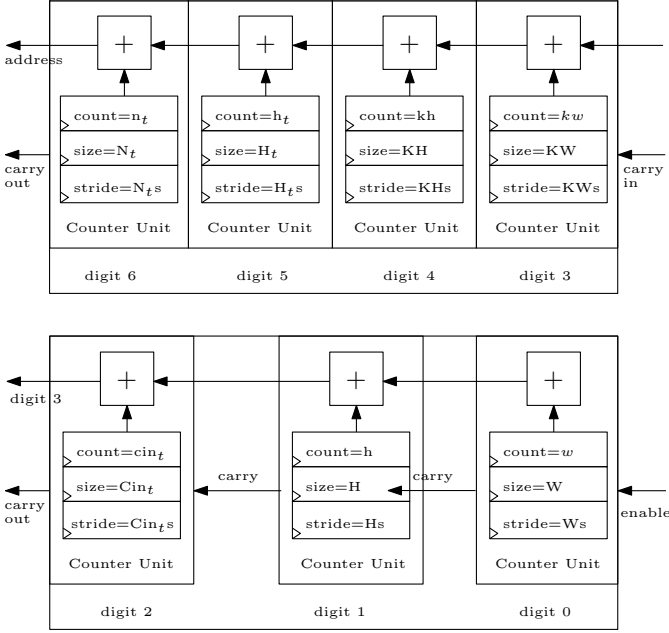


Fig. 5: Layer IO memory access counters for performing in-place mapping of 2-D convolution to GEMM.

is important to integrate the FFIP architecture in a full-system implementation to fully assess the end benefits at the application level. Furthermore, our goal is to validate the benefits of FFIP when overlaid on top of systems based on the most efficient systolic array accelerators used in practice. Therefore, the high-level organization of our system design shown in Fig. 4 *intentionally* shares similarities with the TPUv1 [5] and some similarities with the TPUv2-TPUv4 as well [6] [8]. Based on this, we provide here the system-level implementation we used for the sake of completeness and for better understanding of the context in which our main contributions have been validated.

5.1 Memory Subsystem

The memory accesses are controlled by multi-digit counters (also referred to as tilers) shown in Fig. 5 containing programmable digit sizes and strides which calculate GEMM read/write patterns, as well as map two-dimensional convolution to matrix multiplication to perform Algorithm 1 for any matrix or convolution window sizes without requiring a stand-alone memory remapping stage. The size and strides for each layer are calculated offline once per neural network, and then can be re-used for all inferences of the same neural network after that where they are updated in the memory tilers in real time between each layer. The tilers allow the Memory Unit and external dynamic random-access memory (DRAM) to be interfaced from the Arithmetic Unit using simple first-in first-out (FIFO) interfaces.

The convolutional layer inputs consist of three dimensions, depth C_{in} , height H , and width W . The C_{in} and H dimensions are each split into two separate dimensions to divide them into tiles, and a dimension with the $_t$ subscript denotes the number of tiles in that dimension (e.g. the H dimension is split into H_t tiles each of a new smaller size H). Consider that KH and KW stand for the height and

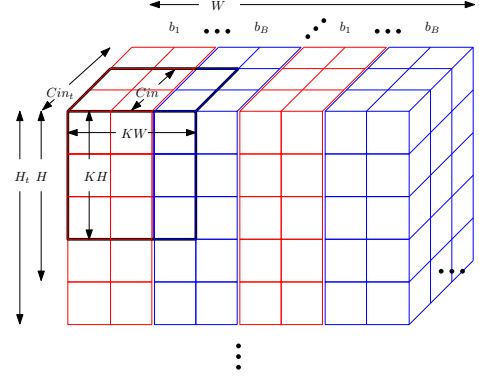


Fig. 6: Layer IO memory access and blocking scheme to partition the memory and perform in-place mapping of two-dimensional convolution to GEMM, provided for context.

Algorithm 1 Layer IO memory access pattern implemented in the counters from Fig. 5 for in-place mapping of 2-D convolution to GEMM, provided for the sake of completeness.

```

1: for  $n_t = 0; n_t < N_t \cdot N_t s; n_t += N_t s$ 
2:   for  $h_t = 0; h_t < H_t \cdot H_t s; h_t += H_t s$ 
3:     for  $kh = 0; kh < KH \cdot KH s; kh += KH s$ 
4:       for  $kw = 0; kw < KW \cdot KW s; kw += KW s$ 
5:         for  $cin_t = 0; cin_t < C_{in_t} \cdot C_{in_t} s; C_{in_t} += C_{in_t} s$ 
6:           for  $h = 0; h < H \cdot H s; h += H s$ 
7:             for  $w = 0; w < W \cdot W s; w += W s$ 
8:                $k_{offset} = kh + kw + cin_t$ 
9:                $m_{offset} = h_t + h + w$ 
10:               $address = m_{offset} + k_{offset}$ 
11:            end for
12:          end for
13:        end for
14:      end for
15:    end for
16:  end for
17: end for

```

width of the kernel size, that a dimension suffixed with s represents the dimension's stride (e.g. W_s is the stride for the W dimension), and N_t stands for the number of tile columns in the B /weight matrix. The convolution is then mapped in-place to GEMM as shown in Algorithm 1 where all of the layer input dimensions are mapped to tiled matrices by mapping each dimension to either a K or M dimension. Similarly, the weight dimensions are tiled and mapped to either the K or N dimensions for GEMM. Each memory location contains X elements along the C_{in} dimension, where X is the MXU width.

5.1.1 Memory Subsystem Timing Optimizations

It was initially found that the maximum frequency of the memory access control counters was lower than the GEMM Unit clock frequency, which would lower the throughput of the entire accelerator and restrict the full frequency advantages of FFIP from being properly evaluated. To resolve this, we partitioned the Layer IO memory into submemories each containing a block of the total memory and separate memory tiler controllers. This allowed each memory block to be accessed concurrently at a slower clock speed and for their read data to then be accessed in an interleaved manner by the main clock.

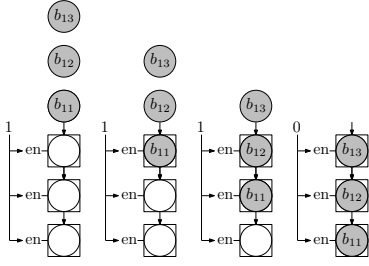


Fig. 7: MXU weight column shift register logic requiring control signal to be connected to each element in the column.

To do this, we derived a memory partitioning scheme for dividing the convolutional layer inputs into blocks in a way that still supports in-place remapping of two-dimensional convolution to GEMM as described above. The partitioning scheme supports dividing the memory into B blocks for any B that is a power of 2, allowing the memory tiler controllers to run at a frequency of $1/B$ times the main clock frequency. In our results, we use $B = 2$. The W dimension is divided into different blocks as show in Fig. 6, where each W slice is W_s elements wide.

One remaining issue, however, is that when the KW dimension increments to a certain range, the submemory may need to access elements from a block that it does not contain. For example, consider the case in Fig. 6 where $kh = kw = 3$, $H_s = W_s = 2$, and $B = 2$. When $kw \in \{1, 2\}$ then element 1 in block 1 will be accessed by the main clock for $w = 1$ followed by element 1 in block 2 for $w = 2$. However, when $kw = 3$ then the block 1 submemory should require access starting with an element from a block that it does not contain. To resolve this, when $kw = 3$ then block 2 will be accessed first by the main memory for $w = 1$, followed by the next block 1 slice for $w = 2$. In other words, the next memory elements are instead taken from the adjacent submemory, the kw and w incremter digits are adjusted in each submemory, and the interleaving order in which the submemories are accessed from the main clock is modified.

We also run the weight memory control logic at a fraction of the main clock speed by accessing the memory in bursts and thus requiring memory control to be communicated to the DRAM controller at an infrequent rate relative to the main clock speed. The external DRAM memory is used only for storing the weights, and the layer inputs/outputs always stay in on-chip memory. This allows the device’s external memory bandwidth to rarely be a bottleneck for the implementations evaluated in our experimental setup discussed in Section 6.

5.2 MXU Timing Optimizations

As discussed in Section 4.3, prior to each tile multiplication, a b/y tile is loaded into the MXU. It then remains in place as the a/g tile flows through the MXU to produce the tile product. As show in Fig. 7, our initial implementation for the mechanism which shifts b/y tiles into the MXU was to implement a basic one-dimensional shift register vector to shift each column of weights into the MXU, and then have an enable control signal that connects to each element in the vector to stop the shifting all at once when the weight column is fully loaded. However, this required enable control

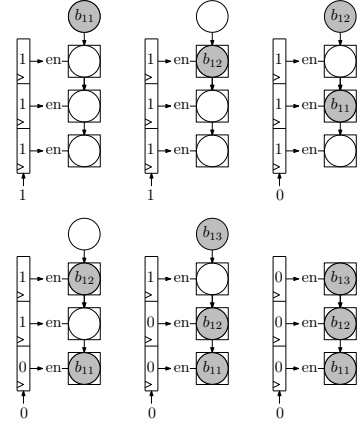


Fig. 8: MXU weight column shift register logic with control connections fully localized to adjacent elements.

signals to be connected non-locally to every element’s shift register enable inputs without being able to locally buffer the enable control signals close to their destinations.

In order to mitigate this, we instead designed an improved shift-register-based mechanism shown in Fig. 8 in which the control signal connections are fully localized by being buffered directly before their destination in each element’s shift register enable input to improve the frequency potential of the MXU. In this design, the control signal has its own shift register mechanism separate from the datapath shift register which is pre-loaded with 1’s. To allow this mechanism, the weights are shifted in every-other clock cycle instead of every clock cycle. Shifting in the weight vectors more slowly like this does not affect the throughput so long as the layer input M_t tile size can usually be at least twice as large as the N_t tile size used for the weights, which was found to be true for the models we used for evaluation.

The key contributions of this work are the proposed FFIP algorithm and architecture and their evaluation in an ML accelerator system, which improve the under-explored FIP [7] that has never before been applied to ML acceleration. Furthermore, our goal is to evaluate FFIP when overlaid on top of a system based on the most efficient systolic array accelerators used in practice. Therefore, this section expanded upon our system design shown in Fig. 4 that *intentionally* shares similarities with the TPUv1 [5] and some similarities with the TPUv2-TPUv4 as well [6] [8], and provides the context in which our main contributions have been validated to better understand their overall impact.

6 RESULTS

This section demonstrates the generality of the FIP-based approaches by evaluating our example (F)FIP implementations on neural networks. The theoretical benefits of the FIP architecture are validated for the first time in a machine learning accelerator. Additionally, we validate the theoretical benefits of the proposed FFIP architecture against the baseline and FIP architectures, and against state-of-the-art prior works. Although the theoretical concepts presented in this work are general and applicable to both custom integrated circuits and field-programmable gate array (FPGA) implementations, our FFIP algorithm and architecture were

validated on FPGA, and we therefore confirm our theoretical insights by comparing the benefits of the proposed FFIP architecture against the best-in-class of prior state-of-the-art ML accelerator solutions that are also evaluated on FPGA. We compare designs for non-sparse neural network acceleration and input sizes quantized to 8 - 16 bits, which are bitwidths commonly used in practice as they provide a balanced trade-off between accuracy versus hardware efficiency [19].

The **source code** for our accelerator implementation is available on GitHub [20] and is hand-coded in SystemVerilog and implemented to be highly configurable. The MXU height/width can be parameterized to be any value that is a multiple of 4. The bitwidth of the a and b values are also fully parameterizable, as well as whether they are on signed versus unsigned representations. The design performs inter-layer rescaling for quantization [19] in the Post-GEMM Unit, which requires an additional Y multipliers (for all MXUs - baseline, FIP, and FFIP). The accelerator has direct memory access (DMA) to the system memory in the host through a Peripheral Component Interconnect Express (PCIe) 3.0 connection. We use a PCIe DMA controller and host driver provided by Xillybus [21]. From the hardware end, the PCIe controller is interfaced through FIFOs. From the software end, the driver is interfaced through shell scripts which we interface with through Python to provide an end-to-end framework for running ML applications on the accelerator.

Full system-level validation of the experimental accelerator system from Section 5 has been done on an Arria 10 SoC Development Kit [22] containing the Arria 10 SX 660 device by measuring model throughput in real-time. However, this device has significantly fewer soft logic resources compared to the Arria 10 GX 1150 used in the majority of the works we compare against on the same FPGA family in this section, and our memory subsystem implementation requires the extra memory resources available in the Arria 10 GX 1150 device for the 16-bit-input architecture. Therefore, in order to provide a comparison with the 16-bit input version of our architecture in Section 6.2.2, and to use the same identical FPGA from the Arria 10 family as the majority of prior works that also use Arria 10, we generate compilation results for our design on the Arria 10 GX 1150 device for a more fair and consistent comparison in Section 6.2.2. The throughput values for our designs on the Arria 10 GX 1150 are calculated using an accurate throughput estimation analysis based on our highly deterministic and time predictable system implementation, which predicts the actual model throughputs measured on the Arria 10 SX 660 device available to us within an error margin of 1% for all MXU sizes. The models used for evaluation are AlexNet [23] and ResNet [24].

6.1 FFIP Compared to Baseline and FIP

The baseline, FIP, and FFIP MXUs from Section 4.3 have been instantiated inside an example accelerator system used for validation that was discussed in Section 5. Different accelerator designs were compiled where the system architecture remained the same, and only the MXU size and type changed. The MXU height/width was incremented by multiples of 8 from sizes 32 to 80, or until the device no

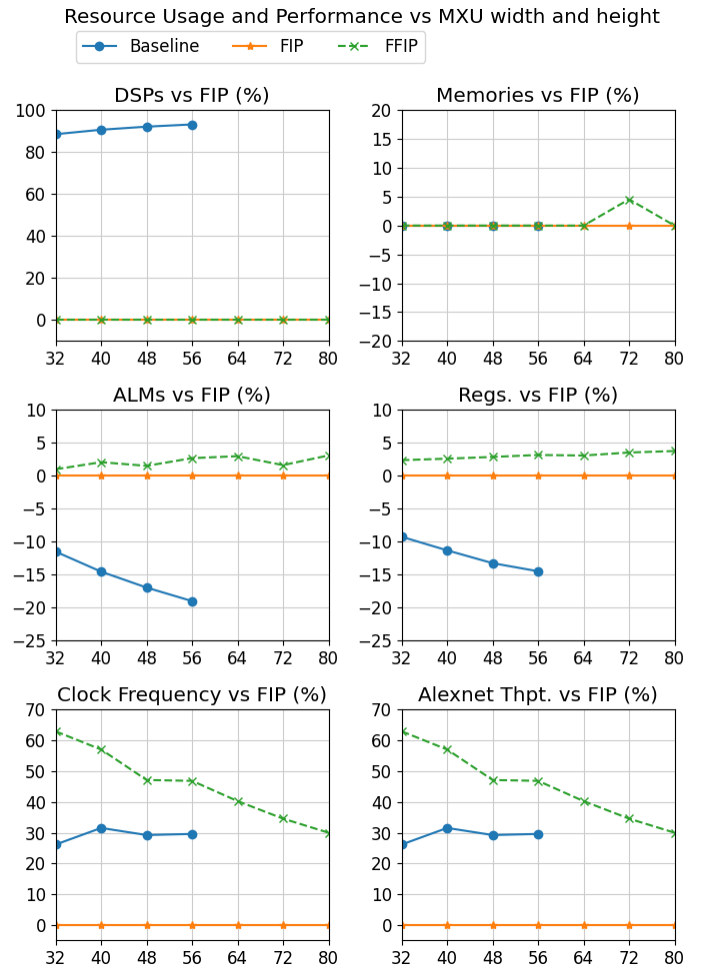


Fig. 9: Evaluating the baseline, FIP, and FFIP MXUs at different sizes instantiated into an example ML accelerator system design used for validation, with 8-bit fixed-point inputs on an Arria 10 SX 660 FPGA.

longer contained enough digital signal processing (DSP) units to instantiate the design. For each MXU size, we compiled a baseline, FIP, and FFIP MXU, except for the baseline MXU designs above size 56×56 which no longer fit on the device due to the DSP resources reaching their limit.

The memory resource deviation seen in the 72×72 FFIP MXU in Fig. 9 is due to the FPGA compiler placing some of the datapath buffers outside of the MXU into memory resources. However, due to the heuristic nature of FPGA compilers, where even bit-equivalent designs will produce small variations in hardware utilizations for different random seeds, this deviation is interpreted as a random outlier and not something inherent to FFIP.

The FIP architecture uses up to 15-20% more ALMs and registers than the baseline to implement the pre-adders that nearly half the multipliers and accumulators are traded for as discussed in Section 4.2. However, as expected from our theoretical analysis, the FIP architecture provides the much more significant **near 2 \times reduction in DSP units**, which are hard logic resources used to implement MAC units in FPGAs since that operation cannot be mapped efficiently

onto the soft logic resources [15]. The clock frequency of the FIP designs, however, is approximately 30% lower than the clock frequency of the baseline designs, which consequently reduces the throughput by the same ratio. As anticipated from our theoretical analysis, the FFIP architecture inherently addresses this weakness of the FIP architecture for a similar hardware cost by maintaining the same near $2\times$ reduction in the number of required DSPs, however, **FFIP improves the clock frequency by over 30%**, and as a consequence, the overall throughput of the accelerator is improved by the same amount compared to FIP. Additionally, the effective size of the largest systolic array that can be fit onto the device before maxing out the DSPs is increased from 56×56 PEs to 80×80 when using FIP and FFIP, a $2\times$ **increase in effective number of PEs**.

Finally, while additional registers could be placed at the FIP PE multiplier inputs to match the critical path of the FFIP PEs, this would come at a significant extra cost in additional registers compared to using FFIP. A detailed analysis for this is provided in Section 4.2.1.

6.2 FFIP Compared to the State-of-the-Art on FPGA

Although the theoretical concepts presented in this work are general and applicable to both custom integrated circuits and FPGA implementations, our FFIP algorithm and architecture were validated on FPGA, and we therefore confirm our theoretical insights by comparing the benefits of the proposed FFIP architecture against the best-in-class of prior ML accelerator solutions that are also evaluated on FPGA.

6.2.1 Performance Metric Definitions and Motivations

The common practice in the field for judging an ML accelerator's performance is with the *effective throughput* metric, op/s , which will also be referred to as solely the *throughput*, and is defined as the number of effective inference operations the accelerator can execute per second in real time. It is also commonly notated as *GOPS* or *TOPS* to represent its value when scaled down by one billion or one trillion, respectively. It is calculated as follows by measuring the average number of inferences performed by the accelerator per second, multiplied by the number of operations required to complete each inference when using traditional algorithms for the algebra such as Eq. (1):

$$throughput = op/s \quad (21a)$$

$$= \frac{\#inferences}{s} \cdot \frac{\#operations}{inference} \quad (21b)$$

$$= \frac{\#operations}{s} \quad (21c)$$

$$\approx \frac{\#multiplications + \#additions}{s} \quad (21d)$$

While there are other operations performed other than strictly additions and multiplications such as the *greater than* operator used in Max-Pool layers, the number of additions and multiplications performed in the majority of ML models dominate the number of other types of operations performed [5], which is why Eq. (21d) is an accurate approximation of Eq. (21c).

Therefore, an accelerator's throughput roof, defined as the throughput if all instantiated compute resources are

utilized in every clock cycle, is accurately approximated by the number of instantiated multiplier and adder units multiplied by how many executions each multiplier and adder unit can perform per second, i.e. the accelerator's clock frequency, as follows:

$$op/s\ roof \approx (\#multipliers + \#adders) \cdot f, \quad (22)$$

where f is the accelerator's clock frequency.

However, the logic complexity of fixed-point multipliers scales quadratically with the input bitwidth compared to linearly for adders and registers, causing the hardware footprint of multipliers to dominate that of adders and registers in the general case [15] [16] [17]. Due to this, multipliers and MAC units are commonly the area-dominant computational resources in ML accelerators [4] [5] [6]. Based on this and the fact that Eq. (1) has the following property:

$$Baseline \ \#additions \approx \#multiplications, \quad (23)$$

we can rewrite Eq. (22) as follows to more directly reflect the computational throughput roof by basing it solely on how many of the area-dominant computational resources, i.e. multipliers, that a device's hardware budget can afford:

$$Baseline \ throughput \ roof = op/s \ roof \quad (24a)$$

$$\approx (\#multipliers + \#adders) \cdot f \quad (24b)$$

$$\approx 2 \cdot \#multipliers \cdot f, \quad (24c)$$

which can also be re-arranged to determine the roof of the following performance per compute area metric:

$$Baseline \ \frac{throughput}{compute \ area} \ roof \approx \frac{op/s \ roof}{\#multipliers} \quad (25a)$$

$$\approx 2 \cdot f, \quad (25b)$$

and the roof of the following performance per compute area per clock cycle metric:

$$Baseline \ \frac{throughput}{compute \ area} \ roof \approx \frac{op/s \ roof}{f} \quad (26a)$$

$$\approx 2. \quad (26b)$$

However, when an accelerator instead uses FIP or FFIP for the arithmetic (Eqs. (2) and (7)), the ratio of multiplications to additions becomes:

$$(F)FIP \ \#additions \approx 3 \cdot \#multiplications. \quad (27)$$

This means that the device can trade nearly half of its compute-area-dominant multipliers for low-area adders while achieving the same throughput and the same number of inferences per second. Since the hardware footprint of the multipliers still dominates that of the adders as explained above, the (F)FIP throughput roof can still be most directly reflected by basing it solely on how many of the area-dominant computational resources, i.e. multipliers, that a device's hardware budget can afford:

$$(F)FIP \ throughput \ roof = op/s \ roof \quad (28a)$$

$$\approx (\#multipliers + \#adders) \cdot f \quad (28b)$$

$$\approx 4 \cdot \#multipliers \cdot f, \quad (28c)$$

which can also be re-arranged to determine the roof the

following performance per compute area metric:

$$(F)FIP \frac{\text{throughput}}{\text{compute area}} \text{ roof} \approx \frac{\text{op/s roof}}{\#\text{multipliers}} \quad (29a)$$

$$\approx 4 \cdot f, \quad (29b)$$

and the roof of the following performance per compute area per clock cycle metric:

$$(F)FIP \frac{\text{throughput}}{\text{compute area}} \text{ roof} \approx \frac{\text{op/s roof}}{\#\text{multipliers}} \quad (30a)$$

$$\approx 4. \quad (30b)$$

Based on the above definitions and reasoning, we use the following three performance metrics for judging prior state-of-the-art solutions against FFIP:

$$\text{throughput} \quad (GOPS) = \text{op/s} \cdot 10^{-9} \quad (31a)$$

$$\frac{\text{throughput}}{\text{compute area}} \left(\frac{GOPS}{\text{multiplier}} \right) = \frac{\text{op/s} \cdot 10^{-9}}{\#\text{multipliers}} \quad (31b)$$

$$\frac{\text{throughput}}{\text{compute area}} \left(\frac{\text{operations}}{\text{multiplier}} \right) = \frac{\text{op/s}}{\#\text{multipliers}} \cdot \frac{1}{f} \quad (31c)$$

For the results in Section 6.2.2, $\#\text{multipliers}$ is calculated as $\#\text{DSPs}$ for AMD/Xilinx FPGAs where each DSP instantiates one 18×27 -bit multiplier [25], and $\#\text{DSPs} \times 2$ for Intel/Altera FPGAs where each DSP instantiates two 18×19 -bit multipliers [26]. The only exception to this is for the works using Intel/Altera FPGAs from Liu *et al.* [27] and Fan *et al.* [28], where two 8-bit multiplications are packed onto each 18×19 -bit multiplier in the DSPs and additional ALMs as explained in Section 6.2.2, and therefore $\#\text{multipliers} = \#\text{DSP} \times 4$.

We also note that, when evaluating solutions on FPGA, it is more common in the field to measure the performance per compute area using $\text{throughput}/\text{DSP}$ rather than $\text{throughput}/\text{multiplier}$. However, we use the latter in order to make the evaluation more generalized and to detach it from the specific DSP architectures currently being used in modern FPGAs. For example, the DSPs on most AMD/Xilinx FPGAs [25] contain one fixed-point multiplier, whereas the DSPs on most Intel/Altera FPGAs [26] contain two fixed-point multipliers, which would make GOPS/DSP comparisons unfair when comparing designs on Intel versus AMD FPGAs, and would decrease the generality of the comparison.

The throughput metric defined in Eq. (31a) measures the raw performance that a solution is able to achieve on a device and is the foremost commonly used metric for comparison in the field. We use the $\text{throughput per compute area}$ and $\text{throughput per compute area per clock cycle}$ metrics defined in Eqs. (31b) - (31c) to help compare the scaling potential of a design regardless of how many computational resources are available on the device it is scaled onto, or so that prejudice is not given towards implementations that could theoretically achieve higher throughputs but did not scale up their design to take full advantage of all the compute resources available on the device. The $\text{throughput per compute area per clock cycle}$ metric serves a similar purpose as $\text{throughput per compute area}$, however, it also normalizes for

clock frequency to further abstract the performance criteria from the implementation platforms and their technology nodes, which will have varying timing potentials, and this metric will also remove any doubt regarding FFIP's performance improvements coming solely from increase in clock frequency compared to the prior works. However, we still include the $\text{throughput per compute area}$ metric because a key benefit of FFIP is that it *does* inherently allow for a higher clock frequency for a similar hardware cost compared to FIP.

6.2.2 Discussion

As derived in Eqs. (24) - (26) versus (28) - (30), (F)FIP increases the theoretical roof of the performance metrics defined in Eqs. (31a) - (31c) in the general case, regardless of the implementation technology. To empirically validate this, we compare our results in this section against the prior state-of-the-art, and since our FFIP algorithm and generalized architecture were validated on FPGA, we confirm our theoretical insights by comparing the benefits of the proposed FFIP architecture against the best-in-class prior solutions also evaluated on FPGA. We demonstrate that FFIP is extremely competitive and surpasses the prior works in the evaluated performance metrics.

Due to the clear advantages, increasing the theoretical limits of the performance metrics defined in Eqs. (31a) - (31c) from Section 6.2.1 has been focused on recently in other works as well. The works by Yopez *et al.* [18] and Jiang *et al.* [31] do this by exploiting Winograd's minimal filtering algorithms applied to convolutional neural networks as shown by the work from Lavin *et al.* [2]. However, as shown in Table 2, the FFIP architectures surpass the prior works in effective ability to reduce the multiplication complexity of the neural network workloads, shown by comparing the $\text{operations}/\text{multiplier}/\text{clock cycle}$ metric defined in Eq. (31c). Furthermore, Winograd's minimal filtering algorithms are applicable only to convolutional layers, whereas FIP and FFIP are applicable to all deep learning models and layer types that mainly decompose to matrix multiplication, such as fully-connected, convolutional, recurrent, and attention/transformer layers. Finally, the Winograd convolution technique [2] still results in matrix multiplication, which can therefore still achieve further compute efficiency improvements by also executing the resulting matrix multiplication on a systolic array architecture housing FFIP PEs.

Additionally, the Arria 10 DSPs [26] can each perform two multiplications between one 18-bit and one 19-bit integer input. As demonstrated in the works by Liu *et al.* [27] and Fan *et al.* [28], it is possible to pack the multiplier inputs such that each 18×19 -bit multiplier performs two multiplications of 6-bit inputs. The remaining two 2×8 -bit multiplications and two 2×6 -bit multiplications required are then performed and summed using extra ALMs. The works by Liu *et al.* [27] and Fan *et al.* [28] use this technique to improve the DSP efficiency for 8-bit inputs. However, this technique requires a noticeable extra cost in ALMs, it is specific to the particular DSP architecture currently being used in Intel/Altera FPGAs [26], and it does not work for 16-bit inputs. We also note that the works from Liu *et al.* [27] and Fan *et al.* [28] report the total resources available on the FPGA in their comparison with prior work, however, we list their total instantiated resources that are also reported in

TABLE 1: Comparison with state-of-the-art 8-bit-input accelerators for different models on the same FPGA family.

	TNNLS '22 [27]		TCAD '22 [28]		Entropy '22 [29]		Ours (FFIP 64×64)			
FPGA	Arria 10 GX 1150		Arria 10 GX 1150		Arria 10 GX 1150		Arria 10 GX 1150			
Data type	8-bit fixed		8-bit fixed		8-bit fixed		8-bit fixed			
ALMs	304K		304K		303K		118K			
Registers	889K		890K		-		311K			
Memories	2334		2334		1953		1782			
DSPs	1473		1473		1503		1072			
Frequency (MHz)	200		220		172		388			
Model	ResNet-50	VGG16	Bayes ResNet-18	Bayes VGG11	R-CNN (ResNet-50)	R-CNN (VGG16)	AlexNet	ResNet-50	ResNet-101	ResNet-152
GOPS ¹	1519	1295	1590	534	719	865	2277	2529	2752	2838
GOPS / ² multiplier	0.258	0.220	0.270	0.091	0.239	0.288	1.062	1.180	1.284	1.324
Operations / ³ multiplier / clock cycle	1.289	1.099	1.277	0.412	1.391	1.673	2.739	3.042	3.310	3.414

¹ Throughput, defined in Eq. (31a), motivation and explanation provided in Section 6.2.1.

² Throughput per compute area, defined in Eq. (31b), motivation and explanation provided in Section 6.2.1.

³ Throughput per compute area per clock cycle, defined in Eq. (31c), motivation and explanation provided in Section 6.2.1.

TABLE 2: Comparison with state-of-the-art 16b-bit-input accelerators for different models on the same FPGA family.

	TCAD '20 [30]			TVLSI '20 [18]		TCAS-II '22 [31]	TCAS-I '23 [32]	Ours (FFIP 64×64)			
FPGA	Arria 10 GX 1150			Arria 10		Arria 10 GX 1150	Arria 10 SoC	Arria 10 GX 1150			
Data type	16-bit fixed			16-bit fixed		8/16-bit fixed ⁴	16-bit fixed	16-bit fixed			
ALMs	286K	335K	208K	181K	180K	-	189K	199K			
Registers	-	-	-	-	-	-	-	530K			
Memories	2356	2692	2319	1310	1310	1565	-	2713			
DSPs	1518	1518	1518	1344	1344	1161	1536	1072			
Frequency (MHz)	240	240	240	250	250	163	200	346			
Model	ResNet-50	ResNet-152	VGG16	VGG16	Modified VGG16	CIPN(VGG +BiLSTM)	Modified StyleNet	AlexNet	ResNet-50	ResNet-101	ResNet-152
GOPS ¹	600	697	968	1642	1788	1224	670	1974	2258	2458	2534
GOPS / ² multiplier	0.198	0.230	0.319	0.611	0.655	0.527	0.218	0.921	1.053	1.146	1.182
Operations / ³ multiplier / clock cycle	0.823	0.957	1.329	2.443 ⁵	2.661 ⁵	3.234 ⁵⁶	1.090	2.659	3.042	3.311	3.413

¹⁻³ See the corresponding definitions from Table 1.

⁴ Weights and layer outputs are quantized to 8 bits. Layer input is quantized to 16-bit due to Winograd convolutional transformations.

⁵ These works use Winograd’s minimal filtering algorithms [2] to reduce multiplication complexity.

⁶ This is a central processing unit (CPU)-FPGA heterogeneous work where portions of the inference are performed on CPU.

their work in our comparison since it is the more common practice and is more favourable for them to use in the comparison here.

We also note that, while our system implementation required more FPGA memory resources than some of the other works, the FFIP architecture proposed in this work affects only to the systolic array of an accelerator and does not consume any of the memory resources itself. The memory subsystem design used in our example accelerator implementation that is consuming the majority of the FPGA memory resources was used to ensure that off-chip memory bandwidth was not a bottleneck on the Arria 10 SoC De-

velopment Kit available to us in order to ensure we could properly evaluate the benefits of FFIP on that platform. FFIP can be used in any accelerator system that uses traditional fixed-point systolic arrays for the arithmetic without fundamentally altering the accelerator’s functionality or internal interfaces in any way, and its usage is orthogonal to the memory subsystem being used in the accelerator.

To make comparisons as fair as possible, we aligned as many variables as possible to the best of our ability in the comparisons in Tables 1 - 3 in regards to making comparisons against implementations on the same FPGA, the same input/datapath bitwidths, and the same ML models.

TABLE 3: Comparison with state-of-the-art accelerators on different FPGAs for the same models and input bitwidths.

	TVLSI '19 [33]	TCAS-II '21 [34]	Ours (FFIP 64×64)	TNNLS '22 [27]	TCAS-I '23 [35]	Ours (FFIP 64×64)	TCAD '20 [30]	Ours (FFIP 64×64)	TNNLS '22 [36]	Ours (FFIP 64×64)	TCAD '20 [30]	Ours (FFIP 64×64)
Model	AlexNet	AlexNet	AlexNet	ResNet-50	ResNet-50	ResNet-50	ResNet-50	ResNet-50	ResNet-101	ResNet-101	ResNet-152	ResNet-152
Data type	16-bit fixed	8/16-bit fixed ⁴	16-bit fixed	8-bit fixed	8-bit fixed	8-bit fixed	16-bit fixed	16-bit fixed	8/16-bit fixed ⁵	16-bit fixed	16-bit fixed	16-bit fixed
FPGA	XC7VX690T	VC709	Arria 10 GX 1150	Arria 10 GX 1150	XCVU9P	Arria 10 GX 1150	Arria 10 GX 1150	Arria 10 GX 1150	VX980	Arria 10 GX 1150	Arria 10 GX 1150	Arria 10 GX 1150
ALMs (Intel) / LUTs (AMD)	468K	121K	199K	304K	-	118K	286K	199K	480K	199K	335K	199K
Registers	649K	160K	530K	889K	-	311K	-	530K	-	530K	-	530K
Memories (20Kb Intel) / (36Kb AMD)	1465	1470	2713	2334	-	1782	2356	2713	1457	2713	2692	2713
DSPs	1436	664	1072	1473	2048	1072	1518	1072	3121	1072	1518	1072
Frequency (MHz)	200	200	346	200	200	388	240	346	100	346	240	346
GOPS ¹	434	220	1974	1519	287	2529	600	2258	600	2458	697	2534
GOPS/ ² multiplier	0.302	0.331	0.921	0.258	0.140	1.180	0.198	1.053	0.192	1.146	0.230	1.182
Operations/ ³ multiplier/clock cycle	1.511	1.657	2.659	1.289	0.701	3.042	0.823	3.042	1.922	3.311	0.957	3.413

¹⁻³ See the corresponding definitions from Table 1.⁴ Weights and layer inputs are quantized to 8 and 16 bits, respectively.⁵ Weights are quantized to 8 bits and layer input/output is quantized to 8 or 16 bits at different stages.

However, since it is not feasible in implementation time to evaluate any one solution for all ML models on all platforms, Tables 1 and 2 compare prior works on the same FPGA family and the same datapath/input bitwidths but for varying ML models. However, since it was not possible to find any more recent prior works evaluated on Arria 10 devices that also evaluate identical ML models as we did, we also provide Table 3, which compares prior works sometimes evaluated on different FPGAs than our validation platform, but for identical ML models and identical or similar input/datapath bitwidths.

Despite the strategies used in some prior works for increasing the theoretical limits of the performance metrics defined in Eqs. (31a) - (31c), the results from Tables 1 - 3, demonstrate that the proposed FFIP approach is the most effective at doing so and can provide performance improvements against the best-in-class prior works in almost all evaluated performance metrics and every evaluated comparison criteria. When comparing the lowest to highest performing models evaluated on FFIP for *throughput per compute area per clock cycle* against the next-most competitive result from the prior works in each table, FFIP is approximately 1.6-2× higher in Table 1, it is overall on-par in Table 2 (even when including the CPU-FPGA heterogeneous system in the comparison [31]), and 1.6-3.7× higher in Table 3. Furthermore, once we account for the higher clock frequency achieved due to the inherent hardware-efficient nature of FFIP, it is further improved over the next-most competitive works in each table, achieving approximately a 3.7-4.6× improvement in Table 1, a 1.4-1.8× improvement in Table 2, and a 2.8-6× improvement in Table 3. Finally,

our FFIP implementation allowed us to achieve the highest overall throughput over the next-most competitive prior works in each table, achieving approximately a 1.4-1.8× improvement in Table 1, a 1.1-1.4× improvement in Table 2, and a 1.7-4.6× improvement in Table 3, allowing us to increase the throughput limits of the evaluation device well beyond its theoretical throughput limits determined by Eq. (24c).

7 CONCLUSION

We present an algorithm and general architecture that improve Winograd’s under-explored inner-product algorithm [7] that can be seamlessly incorporated into any ML accelerator system that uses traditional fixed-point systolic arrays to double the throughput per MAC unit, significantly increasing the accelerator’s performance per compute area across all ML models that will execute on the systolic array.

We implement and evaluate FIP for the first time in a machine learning accelerator system. We then identify a weakness of FIP and propose the new FFIP algorithm and generalized hardware architecture that inherently address that weakness in the general case. We provide ML-specific optimizations for the FIP and FFIP algorithms and systolic array hardware architectures. We derive how the (F)FIP architectures increase the theoretical compute efficiency and performance limits in the general case.

Finally, although the theoretical concepts presented in this work are general and applicable to both custom integrated circuits and FPGA implementations, since our proposed FFIP algorithm and architecture were validated on FPGA, we empirically confirm our theoretical insights

through comparison with prior state-of-the-art solutions also evaluated on FPGA. As anticipated from our theoretical analysis, our full-system validation results shown in Fig. 9 and Tables 1 - 3 confirm that the generalized FFIP systolic array architecture we propose, when implemented, does in fact surpass the traditional theoretical compute efficiency and performance limits, and can improve performance compared to the best-in-class prior state-of-the-art solutions in almost all evaluated performance metrics, each evaluated comparison criteria, and all evaluated ML models. More importantly, our results indicate that FFIP can directly benefit the ML acceleration community by allowing for an increase in the theoretical compute efficiency and performance limitations in the general case across a wide range of devices, system implementations, and ML models.

REFERENCES

- [1] A. Fuchs and D. Wentzlauff, "The accelerator wall: Limits of chip specialization," in *IEEE HPCA*, 2019, pp. 1–14.
- [2] A. Lavin and S. Gray, "Fast algorithms for convolutional neural networks," in *IEEE CVPR*, 2016, pp. 4013–4021.
- [3] S. Winograd, *Arithmetic complexity of computations*. SIAM, 1980, vol. 33.
- [4] X. Liu *et al.*, "WinoCNN: Kernel sharing Winograd systolic array for efficient convolutional neural network acceleration on FPGAs," in *IEEE ASAP*, 2021, pp. 258–265.
- [5] N. P. Jouppi *et al.*, "In-datacenter performance analysis of a tensor processing unit," in *IEEE ISCA*, 2017, pp. 1–12.
- [6] T. Norrie *et al.*, "The design process for Google's training chips: TPUv2 and TPUv3," *IEEE Micro*, vol. 41, no. 2, pp. 56–63, 2021.
- [7] S. Winograd, "A new algorithm for inner product," *IEEE TC*, vol. C-17, no. 7, pp. 693–694, 1968.
- [8] N. P. Jouppi *et al.*, "TPU v4: An optically reconfigurable supercomputer for machine learning with hardware support for embeddings," *arXiv preprint arXiv:2304.01433*, 2023.
- [9] X. Wei *et al.*, "Automated systolic array architecture synthesis for high throughput CNN inference on FPGAs," in *ACM/IEEE DAC*, 2017, pp. 1–6.
- [10] C. Zhang *et al.*, "Caffeine: Toward uniformed representation and acceleration for deep convolutional neural networks," *IEEE TCAD*, vol. 38, no. 11, pp. 2072–2085, 2019.
- [11] O. Gustafsson *et al.*, "Low-complexity general FIR filters based on Winograd's inner product algorithm," in *IEEE ISCAS*, 2013, pp. 93–96.
- [12] L. Elfimova and Y. V. Kapitonova, "A fast algorithm for matrix multiplication and its efficient realization on systolic arrays," *Cybernetics and Systems Analysis*, vol. 37, pp. 109–121, 2001.
- [13] H. Jagadish and T. Kailath, "A family of new efficient arrays for matrix multiplication," *IEEE TC*, vol. 38, no. 1, pp. 149–155, 1989.
- [14] I. Bravo *et al.*, "Different proposals to matrix multiplication based on FPGAs," in *IEEE ISIE*, 2007, pp. 1709–1714.
- [15] K. Guo *et al.*, "[DL] a survey of FPGA-based neural network inference accelerators," *ACM TRETS*, vol. 12, no. 1, pp. 1–26, 2019.
- [16] V. Leon *et al.*, "Walking through the energy-error pareto frontier of approximate multipliers," *IEEE Micro*, vol. 38, no. 4, pp. 40–49, 2018.
- [17] K. Pekmestzi, "Multiplexer-based array multipliers," *IEEE TC*, vol. 48, no. 1, pp. 15–23, 1999.
- [18] J. Yezpez and S.-B. Ko, "Stride 2 1-D, 2-D, and 3-D Winograd for convolutional neural networks," *IEEE TVLSI*, vol. 28, no. 4, pp. 853–863, 2020.
- [19] B. Jacob *et al.*, "Quantization and training of neural networks for efficient integer-arithmetic-only inference," in *IEEE CVPR*, 2018, pp. 2704–2713.
- [20] T. E. Pogue and N. Nicolici, "FFIP accelerator implementation," 2023. [Online]. Available: <https://github.com/trevorpogue/algebraic-nnhw>
- [21] "Xillybus." [Online]. Available: <http://xillybus.com/>
- [22] "Intel Arria 10 SoC development kit." [Online]. Available: <https://www.intel.ca/content/www/ca/en/products/details/fpga/development-kits/arria/10-sx.html>
- [23] A. Krizhevsky *et al.*, "Imagenet classification with deep convolutional neural networks," *Commun. ACM*, vol. 60, no. 6, pp. 84–90, 2017.
- [24] K. He *et al.*, "Deep residual learning for image recognition," in *IEEE CVPR*, 2016, pp. 770–778.
- [25] "UltraScale architecture DSP slice," 2021. [Online]. Available: <https://docs.xilinx.com/v/u/en-US/ug579-ultrascale-dsp>
- [26] "Intel Arria 10 native fixed point DSP IP core user guide," 2017. [Online]. Available: <https://www.intel.com/content/www/us/en/docs/programmable/683583/current/intel-arria-native-fixed-point-dsp-ip.html>
- [27] S. Liu *et al.*, "Toward full-stack acceleration of deep convolutional neural networks on FPGAs," *IEEE TNNLS*, vol. 33, no. 8, pp. 3974–3987, 2022.
- [28] H. Fan *et al.*, "FPGA-based acceleration for bayesian convolutional neural networks," *IEEE TCAD*, vol. 41, no. 12, pp. 5343–5356, 2022.
- [29] J. An *et al.*, "An OpenCL-based FPGA accelerator for Faster R-CNN," *Entropy*, vol. 24, no. 10, p. 1346, 2022.
- [30] Y. Ma *et al.*, "Automatic compilation of diverse CNNs onto high-performance FPGA accelerators," *IEEE TCAD*, vol. 39, no. 2, pp. 424–437, 2020.
- [31] J. Jiang *et al.*, "A CPU-FPGA heterogeneous acceleration system for scene text detection network," *IEEE TCAS-II*, vol. 69, no. 6, pp. 2947–2951, 2022.
- [32] S. Kim *et al.*, "A CNN inference accelerator on FPGA with compression and layer-chaining techniques for style transfer applications," *IEEE TCAS-I*, vol. 70, no. 4, pp. 1591–1604, 2023.
- [33] S. Kala *et al.*, "High-performance CNN accelerator on FPGA using unified Winograd-GEMM architecture," *IEEE TVLSI*, vol. 27, no. 12, pp. 2816–2828, 2019.
- [34] J. Li *et al.*, "An FPGA-based energy-efficient reconfigurable convolutional neural network accelerator for object recognition applications," *IEEE TCAS-II*, vol. 68, no. 9, pp. 3143–3147, 2021.
- [35] D. Kim *et al.*, "Agamoto: A performance optimization framework for CNN accelerator with row stationary dataflow," *IEEE TCAS-I*, vol. Early Access, 2023.
- [36] W. Huang *et al.*, "FPGA-based high-throughput CNN hardware accelerator with high computing resource utilization ratio," *IEEE TNNLS*, vol. 33, no. 8, pp. 4069–4083, 2022.



Trevor E. Pogue Trevor E. Pogue received the B.Eng. degree in Electrical Engineering and the M.A.Sc. degree in Electrical and Computer Engineering from McMaster University, Hamilton, Canada, in 2016 and 2019, respectively. In 2018, he worked as a design verification intern at Synopsys Inc., and in 2022-2023 he worked as an intern at Advanced Micro Devices Inc. He is currently a Ph.D. student in the Department of Electrical and Computer Engineering at McMaster University, Hamilton, Canada. His research interests are in the area of hardware acceleration.



Nicola Nicolici (S'99-M'00-SM'11) Nicola Nicolici (S99-M00-SM'11) received the Dipl.Ing. degree in Computer Engineering from the "Politehnica" University of Timisoara, Romania, in 1997 and the Ph.D. degree in Electronics and Computer Science from the University of Southampton, U.K., in 2000. He is currently a Professor with the Department of Electrical and Computer Engineering, McMaster University, Hamilton, Canada. His research interests are in the area of computer-aided design and

test. He has authored a number of papers in this area. Dr. Nicolici was the recipient of the IEEE TTTC Beausang Award for the Best Student Paper at the International Test Conference in 2000 and the Best Paper Award at the IEEE/ACM Design Automation and Test in Europe Conference in 2004.